Comprehensive study through imaging techniques of the degradation of a resorbable calcium sulphate-based composite bone cement

Open Ceramics 17 (2024) 100542

Contents lists available at ScienceDirect

Open Ceramics

journal homepage: www.sciencedirect.com/journal/open-ceramics

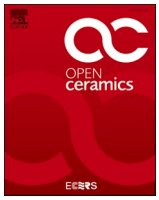

Comprehensive study through imaging techniques of the degradation of a resorbable calcium sulphate-based composite bone cement

Ilaria Corvaglia [a], Ghayadah Alkharusi [b], Federica Banche-Niclot [a], Antonio Manca [c], Tanya J. Levingstone [b,d], Suzanne Little [e], Sonia Fiorilli [a,f], Nicholas Dunne [b,d], Chiara Vitale-Brovarone [a,f,*]

[a] Department of Applied Science and Technology, Politecnico di Torino, Corso Duca Degli Abruzzi 24, 10129 Torino, Italy
[b] Centre for Medical Engineering Research, School of Mechanical and Manufacturing Engineering, Dublin City University, D09 NA55, Dublin, Ireland
[c] Department of Radiology, Candiolo Cancer Institute, FPO-IRCCS, 10060 Torino, Italy
[d] Biodesign Europe, Dublin City University, D09 NA55 Dublin, Ireland
[e] School of Computing, Dublin City University, Dublin, Ireland
[f] National Interuniversity Consortium of Materials Science and Technology, RU Politecnico di Torino, 50121 Firenze, Italy

ARTICLE INFO

Handling Editor: Dr P Colombo

Keywords:
Calcium sulphate resorbable bone cement
Micro-computed tomography
Python

ABSTRACT

The stabilization and treatment of vertebral compression fractures via vertebroplasty procedure foresees the injection of bone cements and recent research is focused on the use of degradable cements featuring an appropriate degradation kinetics. This study presents an investigation into the degradation behaviour of a resorbable ceramic composite cement based on calcium sulphate hemihydrate (CSH), supplemented with strontium-containing mesoporous bioactive glasses (Sr-MBG) and zirconia nanoparticles (ZrO_2). The alterations in the material's microstructure resulting from the degradation process were thoroughly analysed using two image analysis techniques. Micro-computed tomography (Micro-CT) was employed for scanning, while CT-An software associated with the instrument and a Python-coded image analysis tool were utilised to assess porosity and pore size distribution over time. Comparative analysis of the obtained results demonstrated the efficacy of both techniques in comprehensively understanding the internal microstructural changes and volume variations during the degradation of the ceramic composite cement.

1. Introduction

Vertebral compression fractures (VCF) have increased in recent years and are estimated to occur at a prevalence of 10.7 per 1000 per annum in women and 5.7 per 1000 in men in the European population [1]. These fractures cause back pain that can extend to the front of the body [2] and severely impact the patient's quality of life. VCF result in a significant loss of vertebral body height and can make it difficult to maintain proper posture when multiple fractures are present. This condition can lead to a progressive kyphotic deformation of the spine, chronic pain, and potential degeneration and fracture of adjacent vertebral segments [2]. The choice of treatment for VCF depends on the patient's health status and the nature of the fracture, with minimally invasive surgical techniques like vertebroplasty (VP) being commonly preferred [3,4]. VP involves percutaneously injecting a viscous cement paste that hardens over time, stabilising the fractured vertebral body. VP has gained popularity in clinical practice over the past fifty years due to its safety, low invasiveness, and minimal costs compared to traditional surgical procedures [5].

The biomaterials used in VP are injectable bone cements that enhance the strength and stability of the fractured vertebral body, reducing micromotion and alleviating patient's pain. Injectable bone cements consist of dry powder phases and a liquid phase that, when mixed, form a viscous paste that can be injected directly into the fractured vertebral body, where it solidifies. These biomaterials must meet several criteria, including biocompatibility, injectability, and mechanical properties matching those of trabecular bone (e.g., a compressive strength ranging between 2 and 12 MPa) [6]. Additionally, they need to have sufficient radiopacity to enable visualisation during the fluoroscopy-guided surgical procedure. This radiopacity is usually achieved by incorporating zirconia dioxide (ZrO_2) or barium sulphate ($BaSO_4$) particles into the cement formulation [7]. Additionally, there

* Corresponding author.
E-mail address: chiara.vitalebrovarone@polito.it (C. Vitale-Brovarone).

https://doi.org/10.1016/j.oceram.2024.100542
Received 27 July 2023; Received in revised form 10 January 2024; Accepted 15 January 2024
Available online 26 January 2024

are commercial CSH-based products such as Cerament® (BONESUPPORT, Lund, Sweden) that is enriched with an iodine-based liquid phase to confer radiopacity. Bioactivity, defined as the ability of the biomaterial to chemically bond with living bone tissues [8], is also considered highly desirable to enhance osteointegration but is commonly not provided by traditional PMMA-based cement.

The cements used in VP can be classified into two categories based on their interaction with the physiological environment: inert cements, such as acrylic cement based on poly(methyl methacrylate) (PMMA) [9], and resorbable and bioactive cements based on calcium phosphates (CPC) [10,11] and calcium sulphates (CSC). To date, the most frequent bone cements used in vertebroplasty are acrylic ones based on PMMA due to remarkable mechanical performance [12]. Several PMMA-based cements are on the market (e.g., *Osteobond* (Zimmer, Warsaw, IN), Simplex P (Stryker Orthopaedics, Mahwah, NJ, USA), *Fixos* (Transysteme, Nimes, France), *Codman Cranioplastic* (CMW-DePuy), *SpineplexW* (Stryker-Howmedica), *Corinplast* (Corin), *SimplexW P* (Stryker-Howmedica), *PalacosWLV* (Zimmer/Heraeus Kulzer), *KyphXW* (Kyphon), *HV-R* (Kyphon), *OsteopalW* (Heraeus Kulzer), *SymphonyTM VR* (Advanced Biomaterial Systems), *Osteopal V* (Heraeus Kulzer GmbH, Wehrheim, Germany). CPC and CSC are particularly interesting because of their ability to actively interact with the body and gradually get replaced by newly formed bone tissue. They are employed in orthopaedic field since the early 1980s thanks to their excellent biocompatibility and their similar crystallinity and chemical composition to the inorganic component of human bone tissue, especially calcium phosphates [13]. The degradation of these cements primarily occurs through bioerosion processes, which involve the solubilisation of the material's structural network by body fluids and enzymatic bond cleavage by cells [11]. The degradation rate of calcium-based cements is crucial, as it should be complementary to bone regeneration to ensure mechanical reinforcement. If the cement degrades too quickly, long-term support cannot be provided [14,15]. Therefore, a comprehensive understanding of the degradation kinetics of the implanted biomaterial is necessary. Ideally, the cements should be metabolically degraded within several weeks to months [16], aligning with the timeframe of bone tissue regeneration. Another distinction among cements for VP is their "setting mechanism," which refers to the process by which the cement hardens. PMMA cements polymerise rapidly and exothermically due to the presence of a polymerisation initiator in the powder phase [17]. In contrast, the setting mechanism of CPCs and CSCs spontaneously occurs at a physiological temperature of 37 °C through a dissolution/hydration-precipitation process, which can be macroscopically observed by a gradual hardening of the cement paste. Briefly, upon the mixture of the calcium salt powders with the liquid phase, the setting process is initiated by the hydrolysis and dissolution of CPC components and, on the other hand, with the hydration of CSH particles [18]. These initial crystals grow to create a polycrystalline solid, and the final mechanical properties depend on the interconnection of the crystals. Unlike PMMA-based materials that require an initiator, the setting reaction of calcium-based cements relies on the different solubility of the starting crystalline phase and the precipitated one. These characteristics, combined with their resorbable and bioactive properties that support bone tissue regeneration, make calcium-based cements more appealing than the traditional polymeric ones.

A novel class of biomaterials used in VP that gained an increased interest in the past few years is composite cements which aim to improve the performance of individual polymer and ceramic matrices. The focus is on modulating the degradation kinetics and the mechanical properties, as reported by Nilson et al. [19], enhancing bioactivity [20], and, according to Pu et al., improving injectability [21]. These goals can be achieved by incorporating inorganic or organic phases. One promising option is the use of mesoporous bioactive glasses (MBG) particles in the cement formulation, as demonstrated by previous studies [22,23]. Notably, MBG has excellent biocompatibility and the ability to form hydroxyapatite at the interface with the biological environment, promoting stable bonds with bone tissues [24]. Additionally, therapeutic ions such as copper, silver, and strontium can be easily incorporated into MBG, providing specific biological functions [25–29].

In this context, the authors have developed an injectable, resorbable, and composite cement based on calcium sulphate for vertebral body stabilization [22]. This cement combines MBG and commercially available ZrO_2 nanoparticles with a calcium sulphate hemihydrate (CSH) matrix, offering bioactive and radiopacity features, respectively. The incorporation of strontium-containing MBG (Sr-MBG) aims to stimulate bone remodelling and promote pro-osteogenic properties [30,31]. The developed cement has demonstrated suitable properties for VP surgery, including injection and hardening periods as well as mechanical properties within the desired range after injection to the surgical site [22].

Considering the importance of the kinetics of biomaterial degradation for long-term implant success, the present study focuses on a comprehensive analysis of the degradation of the composite cement. The assessment is usually performed under physiological conditions using various media (such as simulated body fluid [32], deionised water [33], phosphate-buffered saline [34] or sodium hydroxide solution [35]) at 37 °C to mimic the physiological conditions. At specific time points, the samples are removed from the media, dried, weighed and the volume reduction is recorded [36]. In addition to weight loss, the external surface of the samples is examined to assess structural and/or compositional changes, and dimensional changes are measured to evaluate macroscale alterations. While these analyses provide preliminary information on sample degradation, they mainly focus on the external surface, lacking detailed insights into internal structural changes and the overall rate of volume reduction.

To address these limitations, the present study proposes a comprehensive analysis of the degradation of an injectable resorbable composite cement consisting of CSH as a resorbable matrix, enriched with ZrO_2 and Sr-MBG nanoparticles for radiopacity and bioactive properties, respectively. The study first assesses the mechanical properties of the cement during the degradation process according to the standard ISO 58233-2002. This evaluation aims to determine whether the compressive strength remains within the typical range of trabecular bone (2–12 MPa) as time progresses [6]. Subsequently, the structural modifications of the composite cement during degradation are evaluated. Traditionally, the degradation of ceramic materials is estimated based on weight or volume loss. However, this study introduces a novel analysis strategy using imaging analysis to investigate structural changes due to degradation. Two image analysis techniques are employed: one based on software associated with a Micro-Computed Tomography (Micro-CT) instrument and the other utilising a Python 3.9-based image analysis tool.

Micro-CT is an advanced imaging technique that enables three-dimensional visualisation and non-destructive analysis of samples at a microscale level [37,38]. It is based on the X-ray absorption of the sample, which depends on its thickness, density, and atomic weight, resulting in images with varying shades of grey [39]. The transmitted radiation is detected by a scintillator detector, which converts it into visible light with an intensity proportional to the radiation energy, and then into a 2D digital image [40]. These 2D digital images are combined to reconstruct the 3D volume of the scanned sample. Due to its superior resolution, Micro-CT is a critical tool in various applications. It is used for quantitative assessment of internal scaffold microstructure, guiding their design and manufacture [41,42]. It also evaluates the microstructural behaviour of multi-phase and fibre-reinforced scaffolds [43,44], and analyses biological samples, particularly bone. Micro-CT has been employed to assess bone quality and structure, study diseases like osteoporosis [38], and estimate the efficacy of preclinical models [45–48]. Additionally, Micro-CT-generated finite element models have been used to predict local plasticity and macroscopic failure of trabecular bone [48,49], evaluate the effects of mechanical stimuli on bone regeneration [50,51], and analyse fluid-structure interactions of bone

marrow within trabecular bone [52]. Furthermore, Micro-CT has been used to assess the changes in various properties of scaffolds and implants over time, particularly regarding degradation and osteointegration of bioprinted scaffolds or metallic implant screws [53,54]. In this study, Micro-CT was used to scan the samples, and the CT-An software associated with the instrument was employed for the analyses. These analyses provided information on porosity, pore dimension distribution, and volume reduction of the samples over time.

While Micro-CT and associated software are widely used for structural analysis, their data analysis tools are limited by the software design. Moreover, collecting data manually involves significant effort, leading to potential inaccuracies due to human error. To overcome these limitations, computer programming languages, such as Python, can be used for data analysis. Python has become one of the most popular programming languages for structural material analysis and data science, capable of handling large datasets. The use of an imaging tool coded in Python offers several advantages. Firstly, it provides flexibility and customisation to the image analysis process, as Python allows for easy modification and adaption of the code to specific needs. Secondly, Python, being an open-source programming language ensures accessibility and cost-effectiveness of the image analysis tool. Lastly, Python's extensive library ecosystem facilitates comprehensive and in-depth analysis of the 2D image data, further enhancing the accuracy of pore size measurement and porosity evaluation in a 2D environment. In this study, an image analysis tool coded in Python 3.9 was employed to evaluate porosity and pore dimension distribution from the reconstructed Micro-CT images of the cement samples. The tool used advanced image processing algorithms to accurately identify and quantify porosity and pore diameter, enabling comprehensive characterisation of the samples. This automated tool simplifies the analysis process, reducing user involvement, and is particularly advantageous when working with extensive datasets [55–58].

The results of this study provide valuable insights into the evolution of cement microstructure and mechanical performance during degradation. To the best of the authors' knowledge, the parallel use and subsequent comparison of two imaging analysis techniques for analysing the degradation of an injectable composite cement have not been explored.

2. Material and methods

2.1. Preparation of the injectable, resorbable composite cement

Cements are prepared by combining a powder phase with a liquid one to create a soft paste. In this study, double-distilled water (ddH_2O) was used as the liquid phase. The powder phase consisted of α-type calcium sulphate hemihydrate (α-CSH; GC Fujirock EP Classic, GC Europe, San Giuliano Milanese, Italy) as a resorbable matrix, along with commercially available ZrO_2 nanoparticles (particle size: 200–500 nm, Anhui Rencheng Technology CO, Hefei, China) and Sr-MBG particles containing 10 mol% of strontium (Si/Ca/Sr = 85/5/10). These components were added to provide radiopacity, bioactive properties, and pro-osteogenic features, respectively. The Sr-MBG particles were prepared using a base-catalysed sol-gel synthesis method previously optimised by the authors [28]. Briefly, an alcoholic solution of tetraethyl orthosilicate (TEOS, Sigma Aldrich, Italy) used as silica-source was added to the aqueous solution containing the surfactants in ethanol, cetyltrimethylammonium bromide (CTAB, Sigma Aldrich, Italy), and the reaction was catalysed with ammonium hydroxide solution. Then, calcium nitrate tetrahydrate (Sigma Aldrich, Italy) and strontium nitrate (Sigma Aldrich, Italy) were added to impart calcium and pro-osteogenic cues to the particles. The solution was allowed to react, and the final nanoparticles were obtained by calcination at 600 °C for 5 h. These bioactive and pro-osteogenic nanoparticles with a size ranging between 100 and 500 nm, presented a great specific surface area and nanopores ranging between 2 and 4 nm [28].

The volumetric formulation of the powder phase of the cement was set at 75 % CSH, 20 % Sr-MBG, and 5 % ZrO_2. To achieve complete injection of the cement, the resulting dry phase was mixed with ddH_2O for 90 s at 20 °C to mimic operating room conditions. The liquid-to-powder ratio (LP) of 0.40 has been previously optimised by the authors [22]. This formulation was designated as 75CSH-MBG, while pure CSH (referred to as 100CSH) was used as the control. After the mixing process, degradation experiments were conducted on cylindrical specimens measuring 13 mm in diameter and 5 mm in height. These specimens were created by extruding the paste through a 13 G needle into cylindrical moulds. The samples were allowed to harden at 37 °C and 100 % humidity for 24 h before further experiments, resulting in the formation of solid cement cylinders.

2.2. Cement morphological characterisation and radiopacity assessment

The surface morphology of the composite cement as well as the distribution of the different nanoparticles in the CSH matrix were assessed by means of Field Emission-Scanning Electron Microscope instrument (FE-SEM; ZEISS MERLIN instrument, Oberkochen, Germany) working at 3 kV acceleration voltage and backscattering mode. The set cement was fixed onto a conductive carbon tape adhered on an aluminium-stub and a 7 nm thick layer of platinum was sputtered to increase sample conductivity. The radiopacity of the cement was evaluated by means of a high-resolution X-ray Micro-CT Skyscan 1272 scanner (Skyscan; Bruker, Ettlingen, Germany) during the scanning phase by detection of the transmitted radiation. The distribution of the radiopaque phase was assessed by maximum intensity projection (MIP) function, specific of CTVox software (Bruker, Ettlingen, Germany). MIP function allows the visualisation of only the most intense voxels in the dataset, hence highlighting the structures of maximum intensity in the sample.

2.3. In vitro degradation test

The degradation behaviour of the cement was evaluated following ISO standard 10999-14. Cylindrical solid cement samples were prepared and immersed in Tris-HCl solution (0.1 M, pH 7.4) at a concentration of 1 g of material per 20 mL of buffer. The samples were placed in an orbital shaker (Excella E24, Eppendorf, Hamburg, Germany) and agitated at 120 rpm at 37 °C for a duration of up to 28 days. Every 7 days, the degradation buffer was completely replaced, and the samples corresponding to the specific time point were collected. These samples were then washed twice with ddH_2O, dried in an oven at 70 °C for 2 h, and the residual weight percentage (residual weight) of each sample was determined as follows:

$$residual\ weight\ (\%) = \left(1 - \frac{w_0 - w_t}{w_0}\right) \times 100$$

where w_0 is the initial weight of the sample (g) and w_t is the weight recorded in the specific time point t (g). The experiments were conducted in duplicate, and results were reported as mean ± standard deviation. Then, the degraded samples were subjected to imaging analyses.

2.4. Mechanical properties

Uniaxial compression tests were conducted on samples collected at various degradation time points, following the guidelines specified in ISO 5833-2002 standard. The compression tests were performed using a Zwick Z5 Testing Machine (Zwick Roell, Genova, Italy) equipped with a 5 kN load cell. Prior to analysis, the diameter of each sample was measured. The compression test involved applying a compressive force to the samples at a displacement rate of 1 mm/min, with a pre-load of 5 N, at room temperature. The samples were positioned on the lower plate of the machine, and a constant-rate compressive load was applied to the

top of each sample until failure occurred. During the test, force and deformation data were collected. The compressive strength was calculated by dividing the maximum load applied to the sample by its cross-sectional area. Triplicate measurements were performed for each formulation at each time point, and the data were reported as the mean value ± standard deviation.

2.5. Scanning of the samples

The microarchitecture of the cement at different time points was analysed using images obtained from a high-resolution X-ray Micro-CT Skyscan 1272 scanner (Skyscan; Bruker, Ettlingen, Germany). The samples were scanned with a 7 μm pixel size, using a voltage of 100 kV and a current of 100 μA. A Cu 0.11 mm filter was applied, and the rotation step was set at 0.3°. Following the scanning phase, image reconstruction was performed using the N-Recon software (Bruker, Ettlingen, Germany).

2.6. Analysis of the data by means of CT-an software

The CT-An software (Bruker, Ettlingen, Germany) was used to extract microstructural parameters from the reconstructed images of the cement samples. The 2D scanned images were reconstructed adopting N-Recon software (Skyscan; Bruker, Ettlingen, Germany). The workflow followed in the process is presented in Fig. 1A. The initial raw images (Fig. 1B) were converted into binary format (threshold set at 40 for 100CSH samples and 30 for 75CSH-MBG samples) to remove the colour scale information (Fig. 1C, left). Customised operations were then applied to address image defects, specifically employing a "despeckle" operation to eliminate black pixels associated with noise (Fig. 1C, right). Finally, 3D analysis was conducted to evaluate the desired parameters, i.e., total volume of the degraded sample, total porosity, pore dimension distribution.

2.7. Pore detection and porosity measurements using image analysis tool

An image analysis function was developed using OpenCV (Python 3.9) to process the images, as schematised in Fig. 2A. The initial step involved collecting the Micro-CT reconstructed images (Fig. 2B). These images were then converted to grayscale and resized to one-fourth of their original size while maintaining their aspect ratio. This resizing was done to eliminate variations in image size that could potentially affect the model's object detection accuracy. Subsequently, a Gaussian filter with a kernel size of 3x3 was applied to reduce noise and enhance the image edges. To convert the images into binary form, Otsu's thresholding method was employed. This method automatically determines an optimal threshold value that separates the pixel intensity histogram into two classes, maximising the variance between them. As a result, the threshold value varies dynamically for each image based on its pixel intensity distribution (Fig. 2C, left). After generating the binary images, morphological operations such as dilation and erosion were applied to remove noise from the object boundaries. The edges of these features were detected using Canny edge detection with threshold values of 1 and 2 (Fig. 2C, right).

Finally, the dimensions of each pore were calculated using contour detection, which measures the distance between pore boundaries. Only contours representing pore areas greater than 800 square pixels (adjusted based on the resized image) were considered in the analysis. Additionally, the code identifies the largest pore, highlights it in the image, and calculates the average pore size. The area of each pore was determined based on the detected contours, and this data was used to calculate the porosity.

3. Results

3.1. Cement characterisation

The main characteristics of the injectable bioresorbable cement were evaluated to assess its potential for VP applications. An ideal cement for VP applications should possess suitable injectability and consistency to prevent leakage, injectability and hardening times compatible with the clinical procedure, and a satisfactory level of radiopacity to be visualised during the surgery. It is also crucial to achieve sufficient compressive strength for mechanical support and degradation kinetics that align with

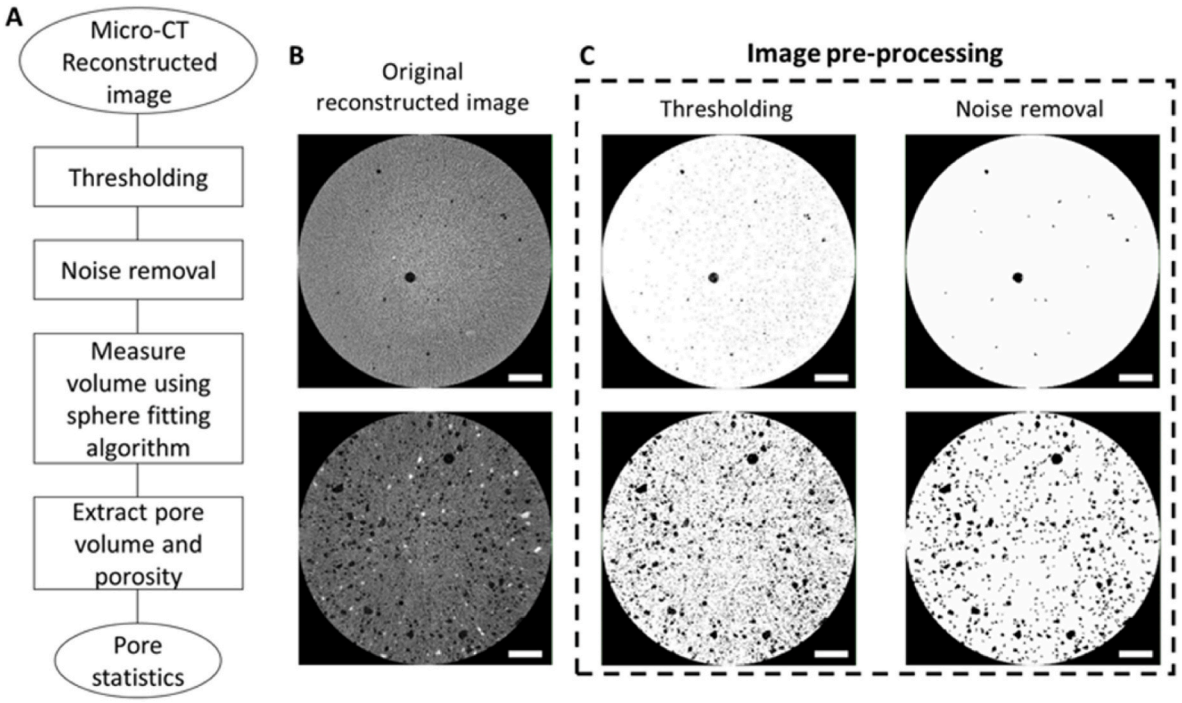

Fig. 1. A: Workflow of custom processing operations performed by Micro-CT CT-An software. B: Raw images of the reconstructed 100CSH (top) and 75CSH-MBG (bottom) formulations. C: Pre-processing methods (thresholding, noise removal) applied to the reconstructed images. Scale bar represents 1 mm.

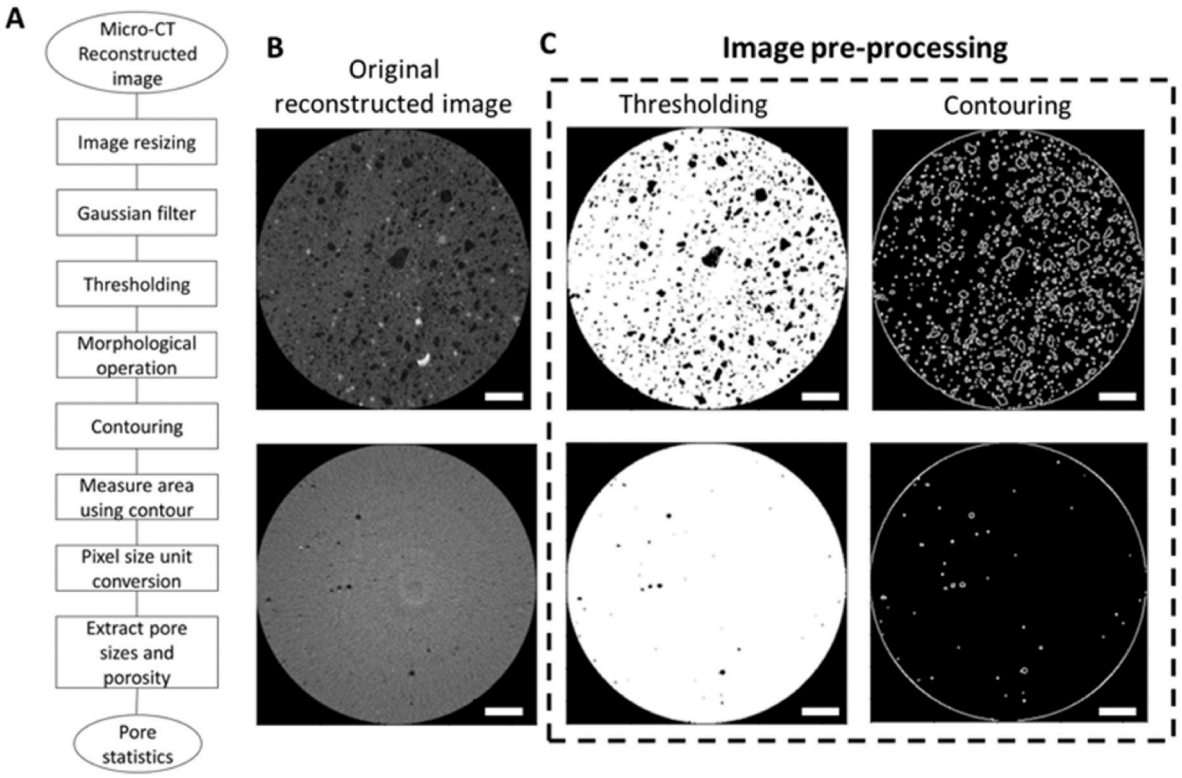

Fig. 2. A: Workflow of the pore detection algorithm coded in Phyton 3.9. B: Raw images of the reconstructed 100CSH (top) and 75CSH-MBG (bottom) formulations. C: Pre-processing methods (thresholding, contouring) applied to the reconstructed images. Scale bar represents 1 mm.

the bone regeneration process. The optimisation of the LP plays a fundamental role in the development of an injectable cement as it directly affects properties such as injectability and final mechanical strength. The 75CSH-MBG cement demonstrated complete injectability through a 13 G needle when an LP of 0.40 was used, resulting in an appropriate consistency of the extruded paste, as shown in Fig. 3A. The time periods for injection (initial setting time) and complete hardened (final setting time) of the cement were determined according to the international standard ASTM C266-04. The developed cement exhibited an initial setting time of approximately 30 min and a final setting time of 60 min (35 ± 2 min and 64 ± 2 min, respectively [22]). These timeframes align with those reported in the literature for composite CSH-based cements [59]. Moreover, the addition of 5 vol% of ZrO_2 nanoparticles provided sufficient radiopacity for the intended clinical application. When the 75CSH-MBG cement was scanned using Micro-CT, no X-ray radiation was transmitted from the central part of the sample to the detector (Fig. 3B), indicating the almost complete absorption of the radiation. This demonstrates the high radiopacity of

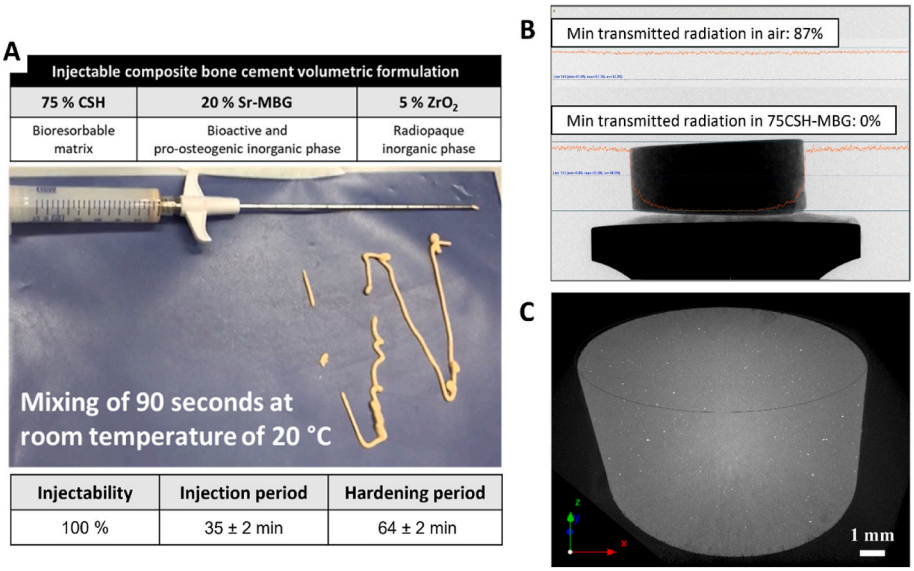

Fig. 3. A: Formulation characteristics and appearance of the 75CSH-MBG cement extruded through a 13G needle. B: Scanning phase of the 75CSH-MBG sample. The minimum transmitted radiation to the detector in air and in presence of the cement is highlighted. C: CT-Vox MIP function of the 75CSH-MBG sample, showing the distribution of the radiopaque phase. The ZrO_2 nanoparticles are represented in white, while the CSH matrix is represented in grey.

the 75CSH-MBG cement, making it suitable for visualisation under VP fluoroscopy surgery. Additionally, the Maximum Intensity Projection (MIP) function, a specific feature of CTVox software associated with the Micro-CT instrument, confirmed the homogeneous distribution of the ZrO_2 nanoparticles throughout the cement volume (Fig. 3C, with ZrO_2 nanoparticles represented as white spots).

Fig. 4 presents representative FE-SEM images of 100CSH control (Fig. 4A–C) and the composite cement (Fig. 4D–F). At a low magnification (1000x), both cements exhibited a uniform morphology with small pores (Fig. 4A and D for the 100CSH and 75CSH-MBG formulations, respectively). Furthermore, at a higher magnification (3000x), the excellent interconnection of the CSH crystals can be observed, resulting in a strong cement (Fig. 4B–C for the 100CSH and Fig. 4E for the composite cement). In the composite cement, the high magnification images confirmed the homogenous distribution of the powders within the CSD matrix, with the ZrO_2 nanoparticles distinguishable due to their whiter colour compared to the cement matrix (Fig. 4E, red arrows). Furthermore, in the cement matrix it is possible to distinguish the presence of Sr-MBG particles at even higher magnifications, characterized by a smaller dimension if compared to the ZrO_2 spherical particles (Fig. 4F, orange arrows).

CSH-based cements per se undergo erosion process once in contact with liquids, e.g., buffer, physiological fluids, leading to their degradation and simultaneous volume reduction over time. The degradation rate of the 75CSH-MBG cement has previously been evaluated by the authors [22], and a representative image is provided in Fig. 5A, along with the corresponding residual weight (Fig. 5B).

3.2. Mechanical properties

The literature extensively demonstrates the importance of matching the mechanical properties of biomaterials with the desired tissue to prevent additional fractures caused by overloading [60]. In the context of VCF, the injected cement should immediately reinforce and stabilise the fractured vertebral body, thereby withstanding cyclic compressive stresses [61]. Furthermore, when resorbable cements are used, they should maintain the provided mechanical support during degradation while facilitating bone tissue regeneration. Based on these considerations, the mechanical properties of the cement were evaluated throughout the degradation process following the ISO 5883-2002 standard to assess whether the compressive strength fell within the range reported for typical trabecular bone (i.e., between 2 and 12 MPa [62]). The compressive strength data collected at Day 0 indicates that the inclusion of ZrO_2 and Sr-MBG nanoparticles resulted in a decrease in compressive strength compared to the 100CSH control, reducing it from 20.1 ± 3.6 to 4.8 ± 1.1 MPa (Fig. 6A). This observation was confirmed through macroscopic examination after the mechanical tests, which revealed a more brittle fracture in the 75CSH-MBG cement compared to the control (Fig. 6B and C). The impact of this brittle fracture can be better understood by considering the measurements of the elastic modulus. The decrease in compressive strength observed in the 75CSH-MBG cement was accompanied by a corresponding decrease in elastic modulus, indicating a more brittle behaviour of the material. Therefore, the inclusion of ZrO_2 and Sr-MBG nanoparticles not only reduced the compressive strength but also affected the elastic behaviour, rendering the material more susceptible to brittle fracture. Furthermore, during the degradation test, the compressive strength values of both investigated biomaterials exhibited a decreasing trend due to erosion caused by the perfusion of the buffer within the samples (Fig. 5). However, it is worth noting that the 75CSH-MBG sample collected at Day 28 unexpectedly demonstrated an increase in compressive strength. This increase can be attributed to the deposition of apatite minerals within the cement matrix. The interaction between the cement and the surrounding environment could have facilitated the deposition of apatite, gradually strengthening the cement matrix over time. Although further investigations are required to confirm this hypothesis, the observed increase in compressive strength suggests a potential contribution of apatite deposition to the mechanical properties of the cement. Overall, the compressive strength of the 75CSH-MBG cement appropriately matches that of trabecular bone tissue [62], demonstrating that the

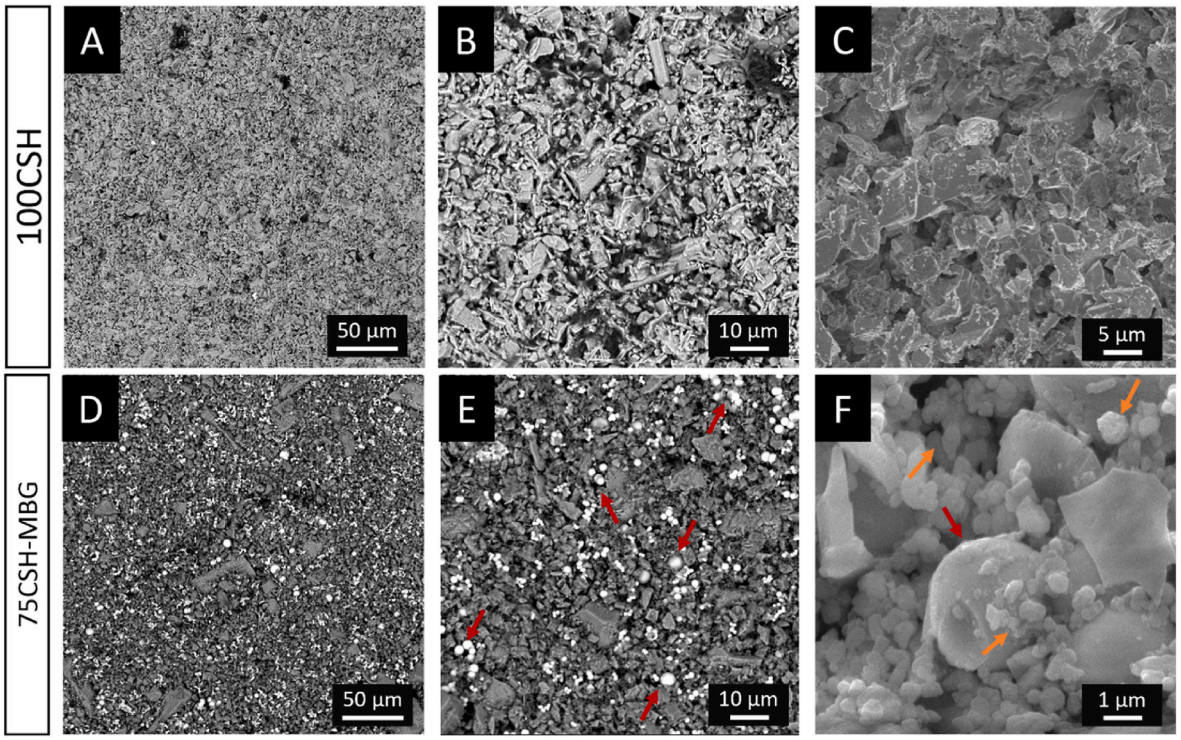

Fig. 4. Representative FE-SEM images of the 100CSH control (A–C) and composite cement 75CSH-MBG (D–E) captured at various magnifications: (A–D) 1000x, (B–E) 3000x and (C–F) 20000x. Red arrows indicate ZrO_2 nanoparticles while orange arrows indicate Sr-MBG nanoparticles.

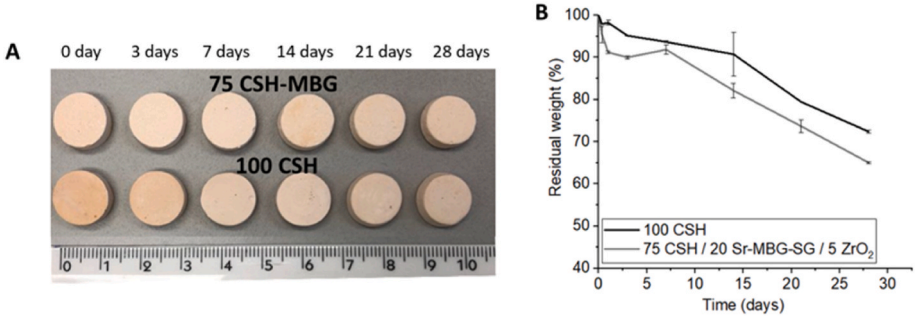

Fig. 5. Degradation kinetics of 75CSH-MBG and 100CSH cements through erosion process (A) and weight loss of samples immersed in Tris-HCl for 28 days (B) [15].

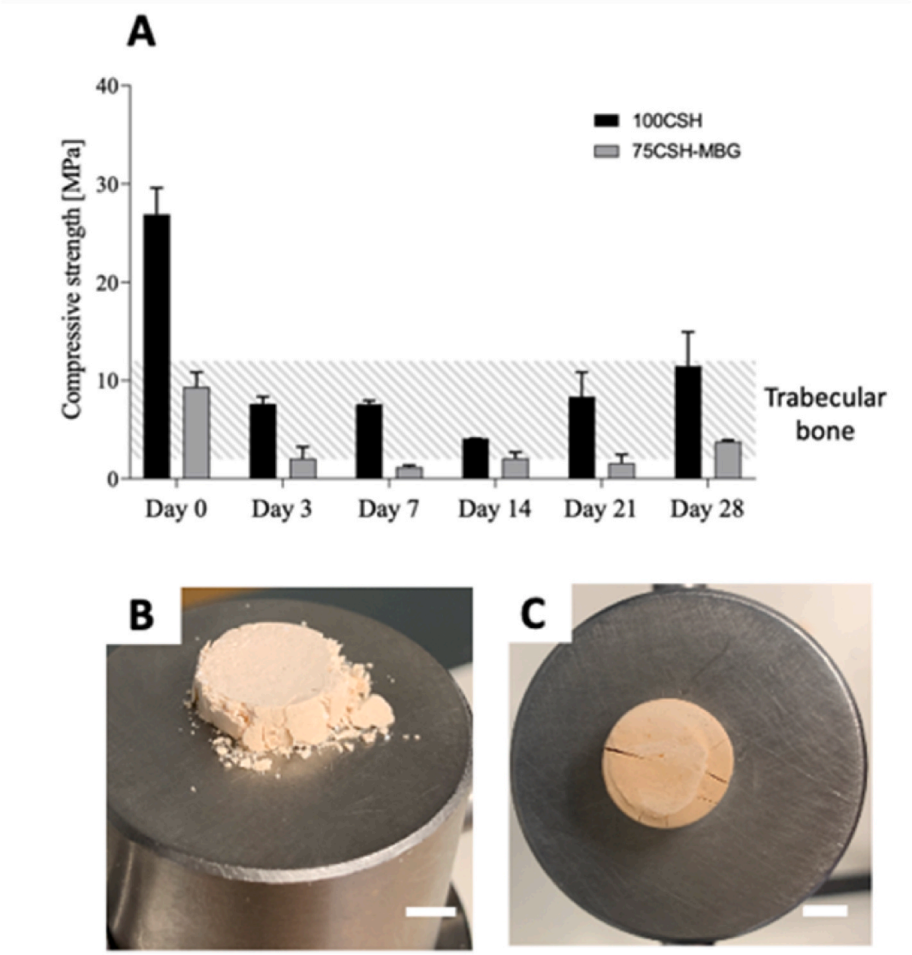

Fig. 6. A: Compressive strength of 100CSH and 75CSH-MBG formulations over time. B: Crack pattern of the 75CSH-MBG formulation at Day 0. C: crack pattern of the 100CSH formulation at Day 0. Scale bar represents 1 mm.

developed CSH-based cement could be a promising candidate for VP applications. While these *in vitro* mechanical experiments have positioned at the lower limit of acceptable values, recent *in vivo* studies conducted by our group and yet unpublished are providing preliminary evidence showcasing the cement's capability to proficiently regenerate bone tissue. Notably, a reinforcement of the cement has emerged attributed to the successful infiltration of regenerated tissue throughout the resorbed biomaterial. These findings not only underscore the cement's potential in bone tissue regeneration particularly in spine applications, but also highlight the synergy and dynamic interaction between the regenerated tissue and the resorbed biomaterial, presenting a promising avenue for further exploration and development.

3.3. Microstructural analysis by means of Micro-CT CT-an software

One important aspect to consider alongside the change in the sample weight during materials degradation is volume reduction. The overall volume reduction over time can be estimated by means of Micro-CT, and the results are presented in Fig. 7A. It can be observed that the 75CSH-MBG formulation reduced its volume by half by Day 28, with a significant decrease of almost 20 % in the first 3 days. The 100CSH formulation showed a more controlled decrease in volume, with a reduction of about 25 % by Day 28. Additionally, the decrease in the sample volume is not solely due to surface erosion processes but also reflects internal structural degradation. This can be observed in Fig. 7B and C, which show the

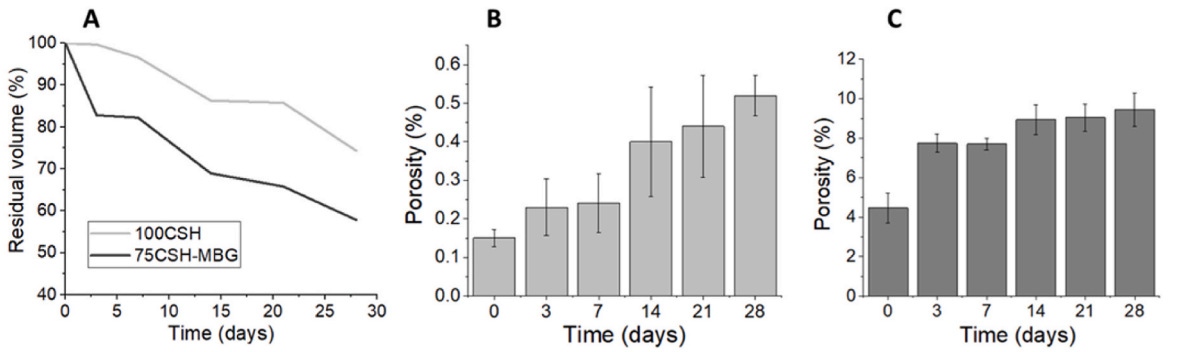

Fig. 7. Microstructural parameters obtained using Micro-CT CT-An software. A: Residual volume for 100CSH (grey) and 75CSH-MBG (black) formulations. B: Percentage of porosity of 100CSH formulation over time. C: Percentage of porosity of 75CSH-MBG formulation over time.

increase in porosity of the cements at different time points. The as-prepared 100CSH formulation had an initial porosity of 0.15 %, which slightly increased after Day 3 and Day 7. At Day 14, the structure's porosity almost doubled and continued to increase up to Day 28, reaching 0.52 % porosity. On the other hand, the 75CSH-MBG formulation had an initial porosity of about 4 %, which almost doubled after just 3 days. Following the initial sharp increase, the porosity continued to rise, reaching a content of approximately 9.5 % by Day 28. The increase in porosity can also be observed in the Micro-CT CT-An images (Fig. S1 and Fig. S2).

Detailed information on the pore size distribution for the 100CSH and 75CSH-MBG formulations is presented in Figs. 8 and 9, respectively. For the as-prepared sample, the 100CSH formulation primarily had pores with diameters in the range of 50–100 μm, and no pores larger than 300 μm in diameter were detected (Fig. 8A). At Day 3, pores with a diameter greater than 300 μm appeared, and their number increased over time. While the percentage of small pores did not significantly change up to Day 14, a high increase in the percentage of small pores (less than 50 μm in diameter) was observed at Day 14.

In the case of the as-prepared 75CSH-MBG formulation, almost 70 % of the pores had diameters ranging between 50 and 100 μm (Fig. 9A). At Day 3, a high percentage of small pores (less than 50 μm in diameter) were present. The percentage of small pores continued to increase by Day 7, while at Day 14, a significant increase of larger pores (with dimensions between 100 and 200 μm) was observed. After Day 14, the pore size distribution did not change substantially.

3.4. Microstructural analysis by means of image analysis tool (Phyton)

Fig. 10A and B present the evaluation of the total porosity over time for the 100CSH and 75CSH-MBG formulations, respectively, using an image analysis tool coded in Phyton 3.9. Both formulations exhibited a

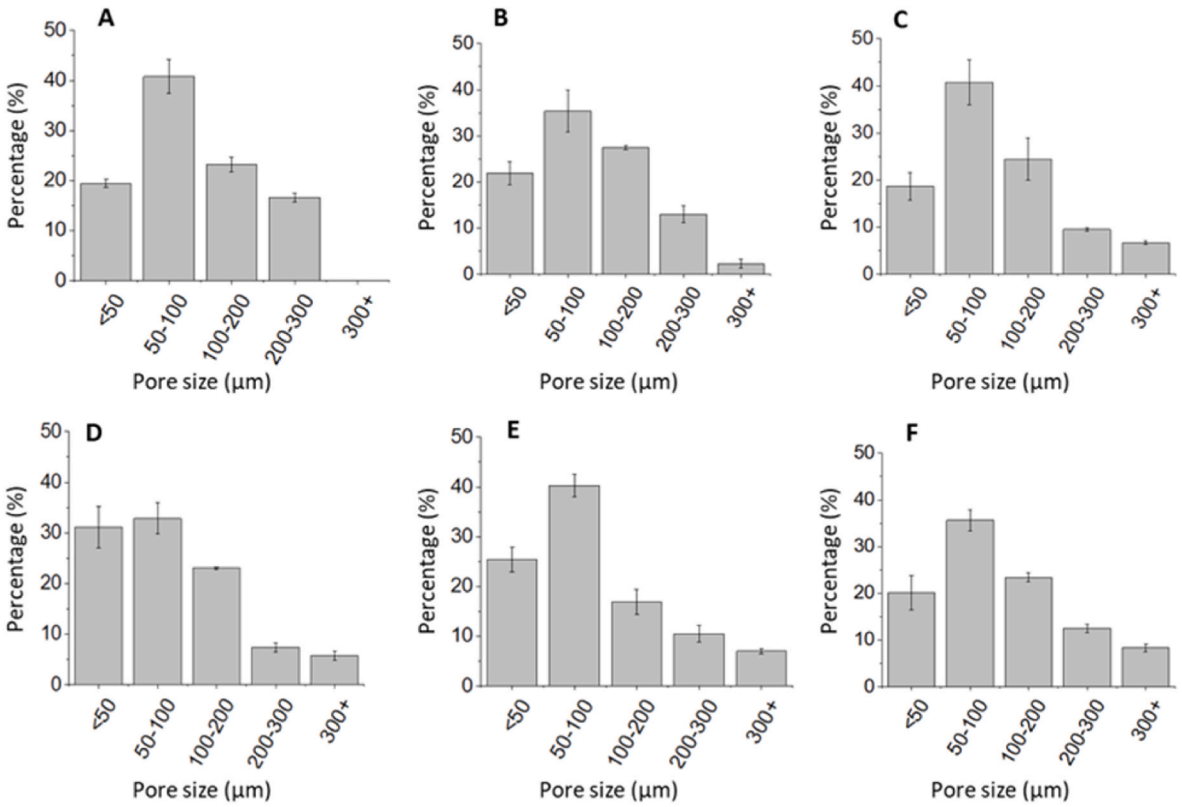

Fig. 8. Pore size distribution over time for 100CSH formulation analysed using Micro-CT CT-An software. A: Initial pore size distribution of the cement. B: Pore size distribution at Day 3. C: Pore size distribution at Day 7. D: Pore size distribution at Day 14. E: Pore size distribution at Day 21. F: Pore size distribution at Day 28.

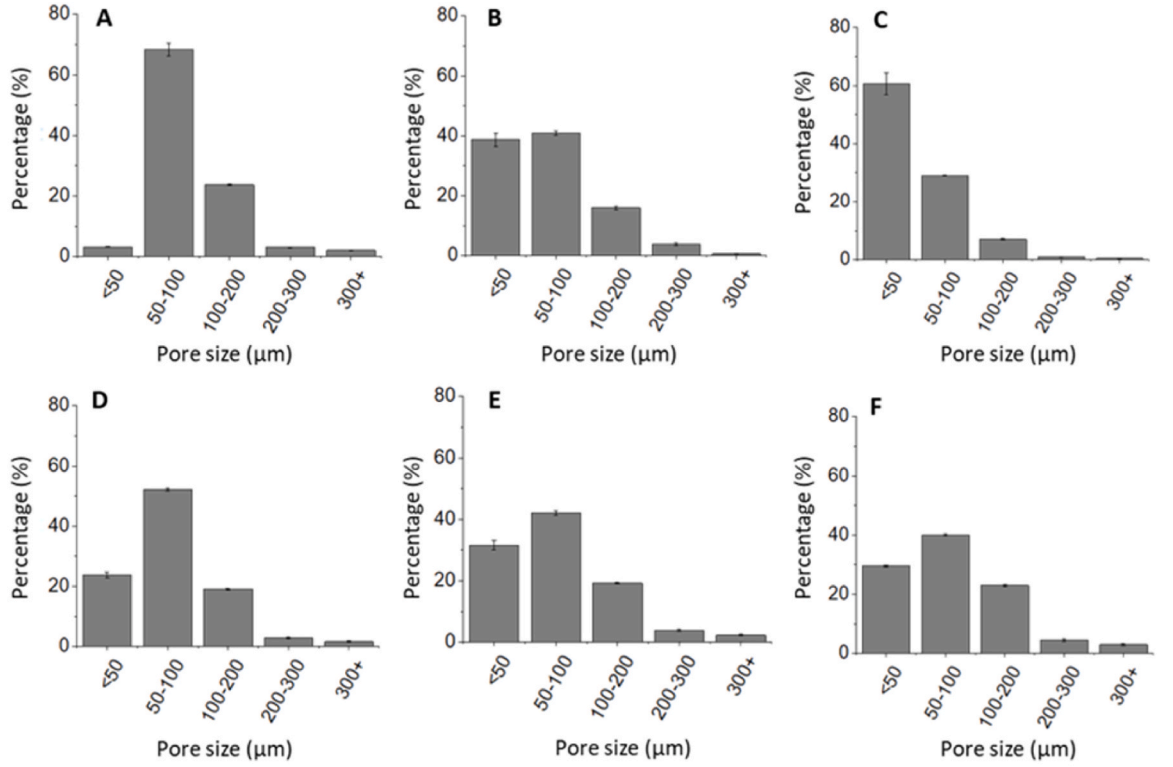

Fig. 9. Pore size distribution over time for 75CSH-MBG formulation analysed using Micro-CT CT-An software. A: Initial pore size distribution of the cement. B: Pore size distribution at Day 3. C: Pore size distribution at Day 7. D: Pore size distribution at Day 14. E: Pore size distribution at Day 21. F: Pore size distribution at Day 28.

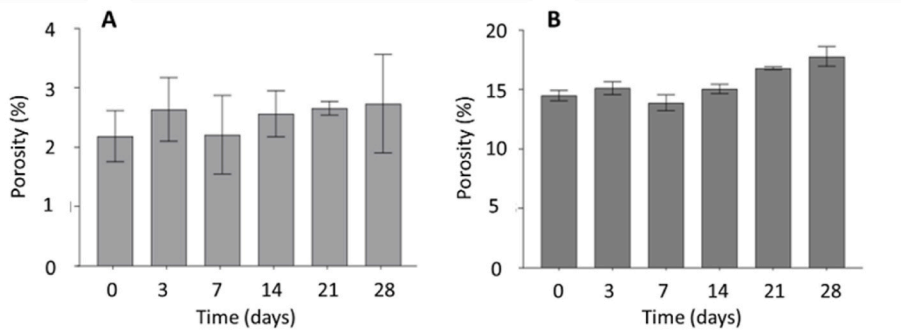

Fig. 10. Microstructural parameters obtained using the image analysis tool. A: Porosity percentage of 100CSH formulation over time. B: Porosity percentage of 75CSH-MBG formulation over time.

slight increase in the total porosity over time. The as-prepared 100CSH formulation had an estimated porosity of approximately 2 %, which increased to about 3 % by Day 28 of immersion in the degradation buffer. Similarly, the as-prepared 75CSH-MBG formulation had a porosity of around 15 %, which increased roughly 18 % by Day 28.

The image analysis tool was also used to assess pore size distribution at different time points. Figs. 11 and 12 present the pore size distribution for the 100CSH and 75CSH-MBG formulations, respectively. The as-prepared 100CSH samples exhibited small pores (below 100 µm), with no pores exceeding 150 µm in diameter detected. The pore size distribution remained relatively unchanged over time, except for the appearance of larger pores (greater than 150 µm in diameter) at Day 14.

In contrast, the as-prepared 75CSH-MBG formulation had a considerable portion of pores below 50 µm in diameter (constituting over 70 % of all detected pores), as shown in Fig. 12. Only a few pores exceeding 100 µm in diameter were observed in the as-prepared samples. As the degradation progressed, the pore size distribution did not undergo substantial changes, with many detected pores remaining below 50 µm in diameter (slightly less than 60 % after Day 28). Like the 100CSH formulation, the presence of larger pores (greater than 100 µm in diameter) was detected by Day 14.

4. Discussion

Information regarding volume reduction and changes in microstructural parameters are valuable for understanding the degradation mechanisms of cement and implanted biomaterials in general. The degradation process of CSH-based materials involves bioerosion process, which occurs due to the solubilisation of the matrix once in contact with physiological liquids and the cellular environment. This process leads to a reduction in material volume from the periphery to the centre [63]. However, evaluating volume changes alone does not consider internal structural variations, such as porosity and pore size distribution. Assessing the porosity of a sample can help correlate these variations

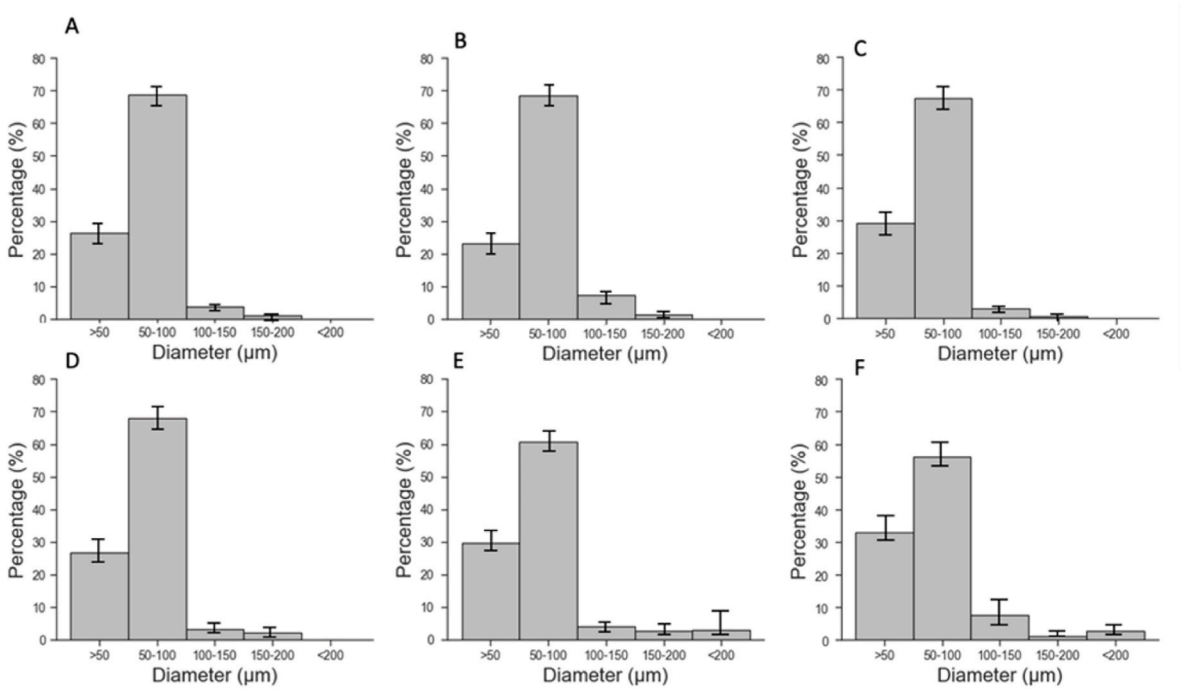

Fig. 11. Pore size distribution over time for 100CSH formulation analysed using image analysis tool. A: Pore size distribution of the cement before degradation testing. B: Pore size distribution at Day 3. C: Pore size distribution at Day 7. D: Pore size distribution at Day 14. E: Pore size distribution at Day 21. F: Pore size distribution at Day 28.

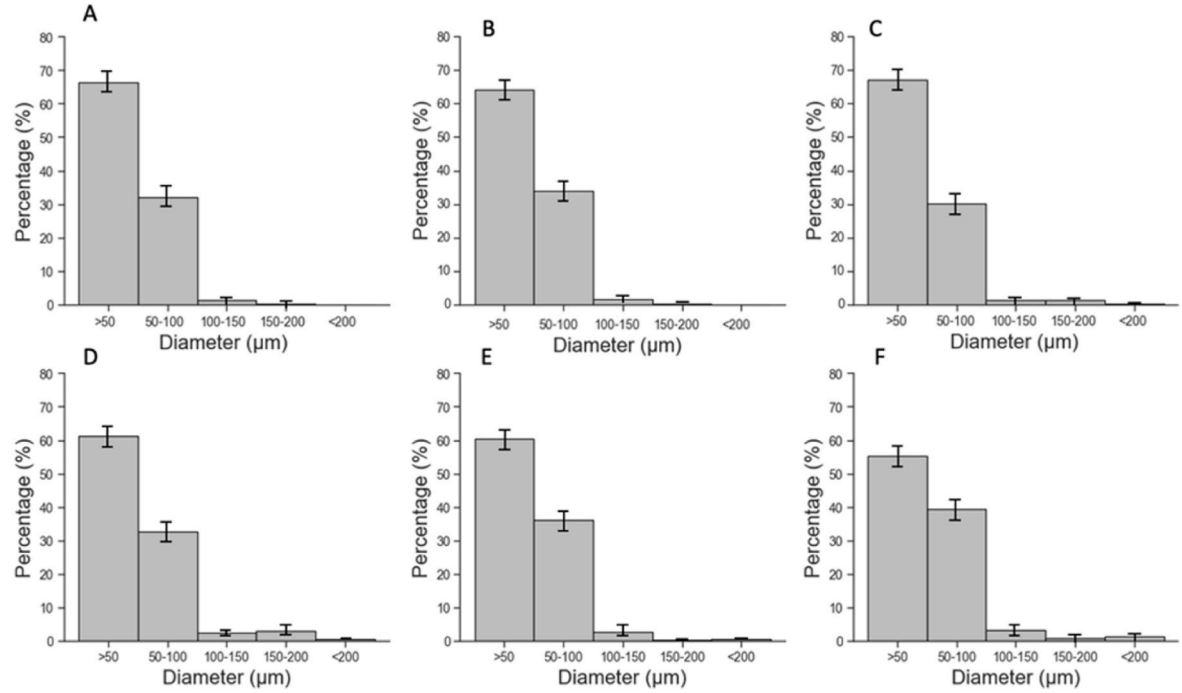

Fig. 12. Pore size distribution over time for 75CSH-MBG formulation using image analysis tool. A: Pore size distribution of the cement before degradation test. B: Pore size distribution at Day 3. C: Pore size distribution at Day 7. D: Pore size distribution at Day 14. E: Pore size distribution at Day 21. F: Pore size distribution at Day 28.

with other features, such as mechanical properties [33]. Understanding pore size distribution is also important for bone regeneration, as the presence of interconnected and large pores can facilitate faster tissue ingrowth and promote replacement of the biomaterial with newly formed tissues [59]. Additionally, the generation of a high number of pores over time exposes Sr-containing MBG particles, which release therapeutic ions upon contact with the biological fluids and enhance osteogenesis.

Micro-CT CT-An software analyses revealed volume reduction in both the 100CSH and 75CSH-MBG formulations, albeit with different

kinetics, particularly by Day 3. The sharp volume reduction for the 75CSH-MBG formulation can be ascribed to its composite nature. In fact, the composite cement formulation includes various components resulting in lower cohesiveness, also evidenced by the declining of the mechanical properties compared to 100CSH. Nonetheless, in the *in vivo* scenario this process is strengthened by the resorption activity of osteoclasts and is accompanied by the deposition of new bone by osteoblasts [64] which allows the upholding of the mechanical support. The less connected structure of the composite cement leads to decreased mechanical properties and increased fluid percolation, resulting in faster degradation on the outer surface and in the internal structure. The composite nature of the 75CSH-MBG formulation also accounts for the different initial porosities compared to the 100CSH. The presence of particles with different granulometry and textural properties [28] in the composite cement increases the incorporation of air during the mixing phase with the liquid, leading to pore formation during extrusion and setting phases. During the immersion period it was observed a general increase in the porosity content that can be linked to the interconnected nature of the samples. Despite the cohesiveness of both 100CSH and 75CSH-MBG formulations, the cement structure is not fully compact, therefore leading to the degradation medium infiltration and consequent internal erosion. Furthermore, the increase in the porosity content over time is reflected in the pore size distribution. 3D morphometric analysis using CT-An revealed that as the total porosity substantially increased (Day 14 for 100CSH and Day 3 for 75CSH-MBG), a considerable increase in the percentage of small pores (below 50 μm) was observed in both cement formulations, as also confirmed in the literature [65]. A slight decrease in the percentage of small pores over time, accompanied by an increase in the percentage of large pores, was also demonstrated by the Python-based imaging tool. This trend indicates internal erosion of the structure, where once a pore is formed, it becomes a new starting point for material degradation, leading to its enlargement through erosion processes. In this study, a gradual increase in the percentage of larger pores was observed, which can be attributed to the low exchange of liquid with the degradation medium compared to the external surface of the cement.

Both Micro-CT software and Python-based image analysis tools have been extensively used in biomaterial and tissue engineering research. However, they are often employed with different focuses. Micro-CT is mainly used for biological assessments, particularly in bone regeneration applications for evaluating new bone formation [66,67]. On the other hand, Phyton 3.9 and relative image analysis tools have been widely exploited for material optimisation, classification, and image segmentation [57]. Only a few studies used Micro-CT, machine learning and algorithms for the evaluation of the degradation kinetics of scaffold [55,68,69].

The two image analysis methods obtained similar results regarding the total porosity and pore size distribution. However, there were differences observed in the pore size distribution of the 75CSH-MBG sample, particularly in the estimation of small pores (less than 50 μm in diameter). To understand these differences, we need to consider the nature of the software and their working processes. Firstly, Micro-CT can analyse the total volume of the sample in its three dimensions, while the Python-based image analysis tool, specifically designed and coded in Python 3.9 for 2D image data analysis, can only work on the 2D slices obtained from the reconstruction phase. Consequently, the Python-based tool calculates pore dimensions in 2D (i.e., area), whereas the Micro-CT CT-An software calculates them in 3D (i.e., volume). Another key distinction lies in the custom processing capabilities of the Micro-CT software, which allows for the removal of disruptive elements present in the images after the reconstruction procedure. In this study, black pixels larger than a specific dimension were eliminated using a "despeckle" operation. These black speckles were detected during the scanning phase and were a result of the complex and dense nature of the sample, causing incorrect distribution of some pixels in the image. By removing and replacing these black speckles generated during the binarization process, the Micro-CT software improved the image quality. The Python-based image analysis tool also includes several pre-processing steps and can perform morphological operations such as erosion and dilation to remove image flaws. However, it is unable to eliminate voids that may be associated with the noise generated during the scanning phase.

These differences in the working methods of the software used can explain the variations in the results. The higher percentage of small pores detected by the Python-based image analysis tool may be attributed to the high sensitivity of the imaging process, which identifies every black spot as a pore. In contrast, during the images preprocessing, CT-An software can remove the defects that will then not be counted during the analysis step. An advantage of using Python is its flexibility and adaptability. The Python code can be modified to specify a minimum pixel size to be identified as a pore. This customisation allows for the exclusion of potential artifacts from the imaging technique, ensuring that only true pores are detected and quantified. Consequently, as all the black speckles are counted as void, the number of small pores (less than 50 μm in diameter) is considerably higher, resulting in a lower fraction of larger pores. Moreover, since the Python-based image analysis tool considers a greater number of pores, the total porosity of the sample is higher compared to the calculation by the CT-An software for both cement formulations. Additionally, the Micro-CT CT-An software can detect and quantify bigger pores (dimension greater than 300 μm) due to its ability to work in a three-dimensional environment. It employs a sphere-fitting approach where the largest possible sphere that can fit within the object is determined [68]. This enables the software to quantify pores with elliptical shapes whose longest dimension is non-horizontal. In contrast, the Python-based image analysis tool, operating in a 2D environment, cannot accurately detect such pores.

Despite the differences in calculation methods between the Python-based image analysis tool and the Micro-CT CT-An software, the results obtained are not markedly dissimilar. Both methods can be considered effective in detecting the sample's porosity and evaluating its pore size distribution.

5. Conclusions

The present study investigated and compared two imaging approaches to comprehensively analyse the degradation behaviour of an injectable, resorbable, composite cement based on CSH. This ceramic-based cement can be used to stabilise VCF and promote bone regeneration. Typically, the degradation of ceramic materials is assessed based on weight or volume loss. However, in this study, two novel strategies focusing on image analysis are proposed and compared to examine the structural changes resulting from the degradation process. The investigated cement formulation consists of a CSH matrix enriched with commercially available ZrO_2 nanoparticles to ensure appropriate radiopacity and strontium containing MBG to enhance the material's bioactivity and pro-osteogenic properties. The mechanical properties of the degrading samples were evaluated by means of testing under compressive loading to ensure that the cement maintains sufficient strength over time. Micro-CT scanning was performed on the degraded cement samples, and image analysis was conducted using Micro-CT CT-An software and a Python 3.9-based image analysis tool. Both analysis techniques were used to assess the changes in microstructural parameters, including total porosity and pore size distribution. The results demonstrated that internal erosion occurs within the samples due to the perfusion of the degradation buffer, leading to an increase in percentage porosity and a general enlargement of pore size. It is worth noting that, to the best of the author's knowledge, the concurrent use and comparison of these two image analysis techniques to analyse the degradation of an injectable composite cement have not been previously explored. Overall, the present work provides detailed information regarding the degradation kinetics of these composite cements, focusing on both the internal and external surfaces of the sample. The study demonstrates that both image analysis methods employed are effective in determining

morphometric features, encompassing overall volume reduction and variations in internal microstructure.

Fundings

This project has received funding from the European Union's Horizon 2020 research and innovation program under grant agreement N° 814410 (GIOTTO https://www.giottoproject.eu/), and by the Science Foundation Ireland (SFI) Centre for Research Training in Artificial Intelligence, Grant number 18/CRT/6223. SL is partly supported by the Science Foundation Ireland (SFI) under Grant Number SFI/12/RC/2289_P2, co-funded by the European Regional Development Fund.

Declaration of competing interest

The authors declare that they have no known competing financial interests or personal relationships that could have appeared to influence the work reported in this paper.

Acknowledgements

The authors are grateful to the JECS Trust for funding (Contract no. 2022294).

Appendix A. Supplementary data

Supplementary data to this article can be found online at https://doi.org/10.1016/j.oceram.2024.100542.

References

[1] D. Felsenberg, et al., Incidence of vertebral fracture in europe: results from the European Prospective Osteoporosis Study (EPOS), J. bone Miner. Res. Off. J. Am. Soc. Bone Miner. Res. 17 (4) (Apr. 2002) 716–724, https://doi.org/10.1359/jbmr.2002.17.4.716.
[2] Y. Dionyssiotis, Management of osteoporotic vertebral fractures, Int. J. Gen. Med. 3 (Jul. 2010) 167–171, https://doi.org/10.2147/ijgm.s11751.
[3] S. Bardají, S. Borrós, New developments in vertebroplasty materials, Afinidad 75 (583) (2018) 165–174.
[4] A.W. Burton, L.D. Rhines, E. Mendel, Vertebroplasty and kyphoplasty: a comprehensive review, Neurosurg. Focus 18 (3) (Mar. 2005) e1, https://doi.org/10.3171/foc.2005.18.3.2.
[5] M.i. S, A.S. Shaikh, Vertebroplasty: a systematic approach, Pain Physician 10 (2007) 367–380.
[6] J.R. Jones, L.M. Ehrenfried, L.L. Hench, Optimising bioactive glass scaffolds for bone tissue engineering, Biomaterials 27 (7) (Mar. 2006) 964–973, https://doi.org/10.1016/j.biomaterials.2005.07.017.
[7] M. Habib, G. Baroud, F. Gitzhofer, M. Bohner, Mechanisms underlying the limited injectability of hydraulic calcium phosphate paste, Acta Biomater. 4 (5) (2008) 1465–1471, https://doi.org/10.1016/j.actbio.2008.03.004.
[8] A. Ruksudjarit, K. Pengpat, G. Rujijanagul, T. Tunkasiri, Synthesis and characterization of nanocrystalline hydroxyapatite from natural bovine bone, Curr. Appl. Phys. 8 (2008) 270–272.
[9] J. Charnley, Anchorage of the femoral head prosthesis to the shaft of the femur, J. Bone Jt. Surg. Br. 42-B (1) (1960) 28–30, https://doi.org/10.1302/0301-620X.42B1.28.
[10] M.A. Goldberg, et al., In situ magnesium calcium phosphate cements formation: from one pot powders precursors synthesis to in vitro investigations, Bioact. Mater. 5 (3) (2020) 644–658, https://doi.org/10.1016/j.bioactmat.2020.03.011.
[11] E. Hughes, T. Yanni, P. Jamshidi, L.M. Grover, Inorganic cements for biomedical application: calcium phosphate, calcium sulphate and calcium silicate, Adv. Appl. Ceram. 114 (2) (2015) 65–76, https://doi.org/10.1179/1743676114Y.0000000219.
[12] P. Galibert, H. Deramond, P. Rosat, D. Le Gars, [Preliminary note on the treatment of vertebral angioma by percutaneous acrylic vertebroplasty], Neurochirurgie 33 (2) (1987) 166–168 [Online]. Available: http://europepmc.org/abstract/MED/3600949.
[13] L.C.C. Brown, W.E. Brown, L.C. Chow, A New Calcium Phosphate, Water-Setting Cement, 1986 [Online]. Available: https://api.semanticscholar.org/CorpusID:99475573.
[14] Y. Kumar C, K.B. N, J. Menon, D.K. Patro, B.H. B, Calcium sulfate as bone graft substitute in the treatment of osseous bone defects, a prospective study, J. Clin. Diagn. Res. 7 (12) (Dec. 2013) 2926–2928, https://doi.org/10.7860/JCDR/2013/6404.3791.
[15] M. V Thomas, D.A. Puleo, Calcium sulfate: properties and clinical applications, J. Biomed. Mater. Res. B Appl. Biomater. 88 (2) (Feb. 2009) 597–610, https://doi.org/10.1002/jbm.b.31269.
[16] P.A. Gunatillake, R. Adhikari, Biodegradable synthetic polymers for tissue engineering, Eur. Cell. Mater. 5 (May 2003) 1–16, https://doi.org/10.22203/ecm.v005a01.
[17] J.C.J. Webb, R.F. Spencer, The role of polymethylmethacrylate bone cement in modern orthopaedic surgery, J. Bone Joint Surg. Br. 89 (7) (Jul. 2007) 851–857, https://doi.org/10.1302/0301-620X.89B7.19148.
[18] R.J. Hand, The kinetics of hydration of calcium sulphate hemihydrate: a critical comparison of the models in the literature, Cem. Concr. Res. 24 (5) (1994) 885–895, https://doi.org/10.1016/0008-8846(94)90008-6.
[19] M. Nilsson, E. Fernández, S. Sarda, L. Lidgren, J.A. Planell, Characterization of a novel calcium phosphate/sulphate bone cement, J. Biomed. Mater. Res. 61 (4) (Sep. 2002) 600–607, https://doi.org/10.1002/jbm.10268.
[20] C.Z.C.G. Zhiwen Pu Hualei Fan, P. Zhu, Effect of bioglass on in vitro bioactivity and cytocompatibility of biphasic α-tricalcium phosphate/gypsum cements, Mater. Technol. 36 (7) (2021) 400–411, https://doi.org/10.1080/10667857.2020.1761654.
[21] Z. Ruan, D. Yao, Q. Xu, L. Liu, Z. Tian, Y. Zhu, Effects of mesoporous bioglass on physicochemical and biological properties of calcium sulfate bone cements, Appl. Mater. Today 9 (2017) 612–621, https://doi.org/10.1016/j.apmt.2017.10.006.
[22] F. Banche-Niclot, et al., Optimization of an injectable, resorbable, bioactive cement able to release the anti-osteoclastogenic biomolecule ICOS-fc for the treatment of osteoporotic vertebral compression fractures, Biomolecules 13 (1) (2023) 94, https://doi.org/10.3390/biom13010094.
[23] M. Dadkhah, et al., Preparation and characterisation of an innovative injectable calcium sulphate based bone cement for vertebroplasty application, J. Mater. Chem. B 5 (1) (2017) 102–115, https://doi.org/10.1039/C6TB02139E.
[24] I. Izquierdo-Barba, M. Vallet-Regí, Mesoporous bioactive glasses: relevance of their porous structure compared to that of classical bioglasses, Biomed. Glas. 1 (2015) 140–150.
[25] V. Mouriño, J.P. Cattalini, A.R. Boccaccini, Metallic ions as therapeutic agents in tissue engineering scaffolds: an overview of their biological applications and strategies for new developments, J. R. Soc. Interface 9 (68) (Mar. 2012) 401–419, https://doi.org/10.1098/rsif.2011.0611.
[26] S. Bose, S. Vahabzadeh, A. Bandyopadhyay, Bone tissue engineering using 3D printing, Mater. Today 16 (12) (2013) 496–504, https://doi.org/10.1016/j.mattod.2013.11.017.
[27] C. Pontremoli, M. Pagani, L. Maddalena, F. Carosio, C. Vitale-Brovarone, S. Fiorilli, Polyelectrolyte-coated mesoporous bioactive glasses via layer-by-layer deposition for sustained Co-delivery of therapeutic ions and drugs, Pharmaceutics 13 (11) (Nov. 2021), https://doi.org/10.3390/pharmaceutics13111952.
[28] S. Fiorilli, et al., Sr-containing mesoporous bioactive glasses bio-functionalized with recombinant ICOS-fc: an in vitro study, Nanomaterials 11 (2) (2021) 1–23, https://doi.org/10.3390/nano11020321.
[29] N. Gargiulo, A.M. Cusano, F. Causa, D. Caputo, P.A. Netti, Silver-containing mesoporous bioactive glass with improved antibacterial properties, J. Mater. Sci. Mater. Med. 24 (9) (Sep. 2013) 2129–2135, https://doi.org/10.1007/s10856-013-4968-4.
[30] E. Gentleman, et al., The effects of strontium-substituted bioactive glasses on osteoblasts and osteoclasts in vitro, Biomaterials 31 (14) (May 2010) 3949–3956, https://doi.org/10.1016/j.biomaterials.2010.01.121.
[31] J. Coulombe, H. Faure, B. Robin, M. Ruat, In vitro effects of strontium ranelate on the extracellular calcium-sensing receptor, Biochem. Biophys. Res. Commun. 323 (4) (Oct. 2004) 1184–1190, https://doi.org/10.1016/j.bbrc.2004.08.209.
[32] I. Yu, S. Kaonis, R. Chen, A study on degradation behavior of 3D printed gellan gum scaffolds, Procedia CIRP 65 (2017) 78–83, https://doi.org/10.1016/j.procir.2017.04.020.
[33] Z. Cai, Z. Wu, Y. Wan, T. Yu, C. Zhou, Manipulation of the degradation behavior of calcium phosphate and calcium sulfate bone cement system by the addition of micro-nano calcium phosphate, Ceram. Int. 47 (20) (2021) 29213–29224, https://doi.org/10.1016/j.ceramint.2021.07.086.
[34] A. Gantar, et al., Nanoparticulate bioactive-glass-reinforced gellan-gum hydrogels for bone-tissue engineering, Mater. Sci. Eng. C 43 (2014) 27–36, https://doi.org/10.1016/j.msec.2014.06.045.
[35] D.F. Coutinho, et al., Modified Gellan Gum hydrogels with tunable physical and mechanical properties, Biomaterials 31 (29) (2010) 7494–7502, https://doi.org/10.1016/j.biomaterials.2010.06.035.
[36] X.D. Li, D.W. Yan, H.H. Ren, Q.Y. Zhang, Y.G. Yan, Fabricating biodegradable calcium phosphate/calcium sulfate cement reinforced with cellulose: in vitro and in vivo studies, J. Mater. Chem. B 11 (2) (2022) 303–315, https://doi.org/10.1039/d2tb02191a.
[37] S.-Y. Chung, J.-S. Kim, D. Stephan, T.S. Han, Overview of the use of micro-computed tomography (micro-CT) to investigate the relation between the material characteristics and properties of cement-based materials, Constr. Build. Mater. 229 (2019) 116843.
[38] A. du Plessis, W.P. Boshoff, A review of X-ray computed tomography of concrete and asphalt construction materials, Constr. Build. Mater. 199 (2019) 637–651, https://doi.org/10.1016/j.conbuildmat.2018.12.049.
[39] G. Molino, G. Montalbano, C. Pontremoli, S. Fiorilli, C. Vitale-Brovarone, Imaging techniques for the assessment of the bone osteoporosis-induced variations with particular focus on micro-CT potential, Appl. Sci. 10 (2020) 8939, https://doi.org/10.3390/app10248939.
[40] C.A.M. Kulak, D.W. Dempster, Bone histomorphometry: a concise review for endocrinologists and clinicians, Arq. Bras. Endocrinol. Metabol. 54 (2) (Mar. 2010) 87–98, https://doi.org/10.1590/s0004-27302010000200002.
[41] E. Saito, D. Suarez-Gonzalez, R.R. Rao, J.P. Stegemann, W.L. Murphy, S. J. Hollister, Use of micro-computed tomography to nondestructively characterize

biomineral coatings on solid freeform fabricated poly (L-lactic acid) and poly ((ε-caprolactone) scaffolds in vitro and in vivo, Tissue Eng. Part C. Methods 19 (7) (2013) 507–517, https://doi.org/10.1089/ten.tec.2012.0495.
[42] J.M. Williams, et al., Bone tissue engineering using polycaprolactone scaffolds fabricated via selective laser sintering, Biomaterials 26 (23) (Aug. 2005) 4817–4827, https://doi.org/10.1016/j.biomaterials.2004.11.057.
[43] S. Lohfeld, et al., Fabrication, mechanical and in vivo performance of polycaprolactone/tricalcium phosphate composite scaffolds, Acta Biomater. 8 (9) (2012) 3446–3456, https://doi.org/10.1016/j.actbio.2012.05.018.
[44] H. Doyle, S. Lohfeld, P. McHugh, Predicting the elastic properties of selective laser sintered PCL/β-TCP bone scaffold materials using computational modelling, Ann. Biomed. Eng. 42 (3) (Mar. 2014) 661–677, https://doi.org/10.1007/s10439-013-0913-4.
[45] N. Abbasi, R.S.B. Lee, S. Ivanovski, R.M. Love, S. Hamlet, In vivo bone regeneration assessment of offset and gradient melt electrowritten (MEW) PCL scaffolds, Biomater. Res. 24 (1) (2020) 1–24, https://doi.org/10.1186/s40824-020-00196-1.
[46] F. Chamieh, et al., Accelerated craniofacial bone regeneration through dense collagen gel scaffolds seeded with dental pulp stem cells, Sci. Rep. 6 (August) (2016) 1–11, https://doi.org/10.1038/srep38814.
[47] A. Sivashanmugam, et al., Injectable shear-thinning CaSO4/FGF-18-incorporated chitin-PLGA hydrogel enhances bone regeneration in mice cranial bone defect model, ACS Appl. Mater. Interfaces 9 (49) (2017) 42639–42652, https://doi.org/10.1021/acsami.7b15845.
[48] E. Verhulp, B. van Rietbergen, R. Müller, R. Huiskes, Indirect determination of trabecular bone effective tissue failure properties using micro-finite element simulations, J. Biomech. 41 (7) (2008) 1479–1485, https://doi.org/10.1016/j.jbiomech.2008.02.032.
[49] N.M. Harrison, P.E. McHugh, Comparison of trabecular bone behavior in core and whole bone samples using high-resolution modeling of a vertebral body, Biomech. Model. Mechanobiol. 9 (4) (2010) 469–480, https://doi.org/10.1007/s10237-009-0188-8.
[50] J.D. Boerckel, Y.M. Kolambkar, H.Y. Stevens, A.S.P. Lin, K.M. Dupont, R. E. Guldberg, Effects of in vivo mechanical loading on large bone defect regeneration, J. Orthop. Res. 30 (7) (2012) 1067–1075, https://doi.org/10.1002/jor.22042.
[51] M. Mehta, S. Checa, J. Lienau, D. Hutmacher, G.N. Duda, "In vivo tracking of segmental bone defect healing reveals that callus patterning is related to early mechanical stimuli.,", Eur. Cell. Mater. 24 (Nov. 2012) 358–371, https://doi.org/10.22203/ecm.v024a26.
[52] T. Sugiyama, L.B. Meakin, W.J. Browne, G.L. Galea, J.S. Price, L.E. Lanyon, Bones' adaptive response to mechanical loading is essentially linear between the low strains associated with disuse and the high strains associated with the lamellar/woven bone transition, J. bone Miner. Res. Off. J. Am. Soc. Bone Miner. Res. 27 (8) (Aug. 2012) 1784–1793, https://doi.org/10.1002/jbmr.1599.
[53] S. Datta, S. Jana, A. Das, A. Chakraborty, A.R. Chowdhury, P. Datta, Bioprinting of radiopaque constructs for tissue engineering and understanding degradation behavior by use of Micro-CT, Bioact. Mater. 5 (3) (2020) 569–576, https://doi.org/10.1016/j.bioactmat.2020.04.015.
[54] D. Krüger, et al., High-resolution ex vivo analysis of the degradation and osseointegration of Mg-xGd implant screws in 3D, Bioact. Mater. 13 (August 2021) (2022) 37–52, https://doi.org/10.1016/j.bioactmat.2021.10.041.
[55] C.L. Reedy, C.L. Reedy, High-resolution micro-CT with 3D image analysis for porosity characterization of historic bricks, Herit. Sci. 10 (1) (2022) 83, https://doi.org/10.1186/s40494-022-00723-4.
[56] G. Lo Re, F. Lopresti, G. Petrucci, R. Scaffaro, A facile method to determine pore size distribution in porous scaffold by using image processing, Micron 76 (2015) 37–45, https://doi.org/10.1016/j.micron.2015.05.001.
[57] N. Hojat, P. Gentile, A.M. Ferreira, L. Šiller, Automatic pore size measurements from scanning electron microscopy images of porous scaffolds, J. Porous Mater. 30 (1) (2023) 93–101, https://doi.org/10.1007/s10934-022-01309-y.
[58] H.Y. Kim, R.H. Maruta, D.R. Huanca, W.J. Salcedo, Correlation-based multi-shape granulometry with application in porous silicon nanomaterial characterization, J. Porous Mater. 20 (2) (2013) 375–385, https://doi.org/10.1007/s10934-012-9607-9.
[59] Ö. Demir-Oğuz, A.R. Boccaccini, D. Loca, Injectable bone cements: what benefits the combination of calcium phosphates and bioactive glasses could bring? Bioact. Mater. 19 (April 2022) (2023) 217–236, https://doi.org/10.1016/j.bioactmat.2022.04.007.
[60] C.R. Rios-Soberanis, S. Wakayama, T. Sakai, J.M. Cervantes-Uc, A. May-Pat, Evaluation of mechanical behaviour of bone cements by using acoustic emission technique, Adv. Mater. Res. 856 (2014) 246–250. https://doi.org/10.4028/www.scientific.net/AMR.856.246.
[61] S. Wu, X. Liu, K.W.K. Yeung, C. Liu, X. Yang, Biomimetic porous scaffolds for bone tissue engineering, Mater. Sci. Eng. R Reports 80 (2014) 1–36, https://doi.org/10.1016/j.mser.2014.04.001.
[62] J.S. Temenoff, A.G. Mikos, Injectable biodegradable materials for orthopedic tissue engineering, Biomaterials 21 (23) (Dec. 2000) 2405–2412, https://doi.org/10.1016/s0142-9612(00)00108-3.
[63] J. Lu, et al., The biodegradation mechanism of calcium phosphate biomaterials in bone, J. Biomed. Mater. Res. 63 (4) (2002) 408–412, https://doi.org/10.1002/jbm.10259.
[64] J. Zhang, L. Wang, W. Zhang, M. Zhang, Z.-P. Luo, Synchronization of calcium sulphate cement degradation and new bone formation is improved by external mechanical regulation, J. Orthop. Res. Off. Publ. Orthop. Res. Soc. 33 (5) (May 2015) 685–691, https://doi.org/10.1002/jor.22839.
[65] L. Yu, et al., A novel injectable calcium phosphate cement-bioactive glass composite for bone regeneration, PLoS One 8 (4) (2013) e62570, https://doi.org/10.1371/journal.pone.0062570.
[66] C.M. Cowan, et al., Adipose-derived adult stromal cells heal critical-size mouse calvarial defects, Nat. Biotechnol. 22 (5) (2004) 560–567, https://doi.org/10.1038/nbt958.
[67] L. Terranova, et al., Repair of calvarial bone defects in mice using electrospun polystyrene scaffolds combined with β-TCP or gold nanoparticles, Micron 93 (2017) 29–37, https://doi.org/10.1016/j.micron.2016.11.001.
[68] N. Alqahtani, F. Alzubaidi, R.T. Armstrong, P. Swietojanski, P. Mostaghimi, Machine learning for predicting properties of porous media from 2d X-ray images, J. Pet. Sci. Eng. 184 (2020) 106514, https://doi.org/10.1016/j.petrol.2019.106514.
[69] M.L. Bouxsein, S.K. Boyd, B.A. Christiansen, R.E. Guldberg, K.J. Jepsen, R. Müller, Guidelines for assessment of bone microstructure in rodents using micro-computed tomography, J. bone Miner. Res. Off. J. Am. Soc. Bone Miner. Res. 25 (7) (Jul. 2010) 1468–1486, https://doi.org/10.1002/jbmr.141.